frontiers | Frontiers in Acoustics

TYPE Original Research
PUBLISHED 11 October 2023
DOI 10.3389/facou.2023.1271221

OPEN ACCESS

EDITED BY
Stefano Laureti,
University of Calabria, Italy

REVIEWED BY
Marco Miniaci,
Swiss Federal Laboratories for Materials Science and Technology, Switzerland
Marco Ricci,
University of Calabria, Italy

*CORRESPONDENCE
Massimo Ruzzene,
massimo.ruzzene@colorado.edu

RECEIVED 01 August 2023
ACCEPTED 28 September 2023
PUBLISHED 11 October 2023

CITATION
Riva E, Rosa MIN, Guo Y and Ruzzene M (2023), Adiabatic sound transport in acoustic waveguides with time-varying Helmholtz resonators.
Front. Acoust. 1:1271221.
doi: 10.3389/facou.2023.1271221

Adiabatic sound transport in acoustic waveguides with time-varying Helmholtz resonators

Emanuele Riva[1], Matheus I. N. Rosa[2], Yuning Guo[2] and Massimo Ruzzene[2]*

[1]Department of Mechanical Engineering, Politecnico di Milano, Milano, Italy, [2]Department of Mechanical Engineering, University of Colorado Boulder, Boulder, CO, United States

We investigate the dynamics of acoustic waveguides with time-varying Helmholtz resonators and the ensuing wave propagation features. We focus on the numerical modeling of such a system with emphasis on the time-varying dispersion properties and emerging wave phenomena due to slow time modulation. We show that a propagating wave packet experiences a transformation that preserves the wavenumber content, resulting in frequency conversion that follows the time evolution of the dispersion bands. The conditions for such a transformation to be "adiabatic" are derived analytically, which allows the identification of the limiting modulation speed required to avoid undesired reflections or mode conversions. The predictions from the dispersion investigations are confirmed by time-domain numerical simulations, which illustrate the possibilities for frequency conversion and temporal signal compression or decompression of impinging signals. The framework presented herein may open new avenues in the context of time-varying phonic waveguides, with possible applications in communication, sound isolation, and frequency conversion.

KEYWORDS

acoustic metamaterials, time-varying waveguides, Helmholtz resonators, frequency conversion, time compression, adiabatic transformation

1 Introduction

The extensive research in metamaterials has investigated intriguing properties to functionally control wave propagation within different physical domains. Various implementations in optical, elastic, and acoustic systems showcase phenomena produced by periodic tessellations of Bragg-scattering or locally-resonant units, which define different bandgap formation mechanisms (Hussein et al., 2014; Cummer et al., 2016; Kadic et al., 2019; Oudich et al., 2023). Following this concept, a number of wave manipulation strategies have emerged to produce attenuation (Liu et al., 2000), localization (Hu et al., 2021), and mode-conversion (Dong et al., 2022), which are of particular relevance for sound and vibration isolation purposes. Other configurations rely on the careful manipulation of spatial symmetries in the creation of back-scattering immune topological waveguides (Ma et al., 2019), including elastic/acoustic analogs to the quantum spin Hall (QSH) (Süsstrunk and Huber, 2015; Miniaci et al., 2018) and quantum valley Hall (QVH) (Pal and Ruzzene, 2017) effects, for example. Another line of work takes advantage of metamaterials with gradually varying

units, which are known to support slow waves (Tsakmakidis et al., 2007; Wang et al., 2023) produced by a gradual decrease of the wave's speed in space, and which may be useful in applications such as energy harvesting (De Ponti et al., 2020) and enhanced sensing (Chen et al., 2014). Acoustic cloaks (Norris, 2008), rainbow trappers (De Ponti et al., 2021), and lenses (Allam et al., 2021) are additional examples where spatial variations of the underlying medium properties are key in providing some degree of wave control.

All the examples above are induced by a modulation of the underlying media in space. However, wave propagation in spatially periodic or spatially varying systems is constrained by frequency-invariant dispersion characteristics. In contrast, time-modulated metamaterials are excellent candidates to broaden the wave control opportunities in the context of metamaterial-based waveguiding. For instance, non-reciprocal wave propagation (Trainiti and Ruzzene, 2016; Marconi et al., 2020), parametric amplification (Trainiti et al., 2019), temporal pumping (Grinberg et al., 2020; Xu et al., 2020; Xia et al., 2021), and temporal waveguiding (Pacheco-Peña and Engheta, 2020b; Santini and Riva, 2022) are behaviors that cannot be met by linear time-invariant interactions. Experiments on this matter have propelled this research topic, establishing itself as an attractive field during active times in phononics (Zangeneh-Nejad and Fleury, 2019).

In this context, we present a framework for the study of wave propagation in time-modulated acoustic metamaterials within the context of an adiabatic theorem. Our analysis is inspired by previous studies on adiabatic transformations of standing modes (Xia et al., 2021), and on adiabatic wave steering in spring-mass lattices (Santini and Riva, 2022). Here, we explore an acoustic waveguide endowed with Helmholtz resonators whose neck cross-section is modulated in time to produce a time-varying resonant frequency. We show that an incident wave packet propagating through the time-varying waveguide undergoes a wavenumber-invariant frequency conversion that follows the time evolution of the dispersion bands. Through the adiabatic theorem, we show that fast, or non-adiabatic, modulations produce leaks from the incident wave packet toward other wave modes. Through this framework, we compute a limiting condition for the modulation velocity which produces frequency conversion through a scattering-free process and we identify the transition between adiabatic and non-adiabatic processes. Supported by the derived adiabatic conditions, our numerical results reveal possibilities for frequency conversion and temporal signal compression or decompression, which may define novel functionalities of metamaterial waveguides enabled by smooth temporal modulations which may otherwise be difficult to realize via purely mechanical or electromechanical configurations (Xia et al., 2021).

This paper is organized as follows. The theoretical aspects are discussed in Section 2, starting from the derivation of the equations of motion and with emphasis on the dispersion analysis and the adiabatic theorem. In Section 3, we report a number of relevant case-studies, where time modulation is tailored to control frequency and mode conversion. Concluding remarks are presented in Section 4.

2 Acoustic waveguides with time-varying resonators: modeling and solution methods

In this section, we describe the modeling of the one-dimensional (1D) acoustic waveguide endowed with time-varying Helmholtz resonators. We first derive the equations of motion of the coupled system, followed by a homogenization in the long-wavelength limit which allows for analytical expressions of the dispersion relations in the absence of time modulation. Finally, we describe the adiabatic conditions for transformations induced by slow time modulation of the resonators' properties, which delineates the transition between frequency conversion with and without energy scattering toward undesired wave modes.

2.1 Equations of motion

We consider a 1D acoustic waveguide of constant cross-section area A, featuring a period array of Helmholtz resonators of volume V, spaced by a distance a (Figure 1). The resonators have a neck length l and neck area $A_r(t)$, the latter assumed to be mechanically varied in time. The wave equation for the acoustic waveguide is expressed as Kinsler et al. (2000):

$$\frac{1}{c^2}\frac{\partial^2 p}{\partial t^2} - \frac{\partial^2 p}{\partial x^2} = \frac{\partial G}{\partial t} \tag{1}$$

where $p = p(x,t)$ is the pressure field along the pipe, c is the speed of sound, and $G(x, t)$ is the apparent rate of input mass per unit volume associated with the resonators. We assume a lumped-parameter model for the resonators, whose only degree of freedom $\psi(t)$ is the outward fluid displacement of the neck, which is constant along the cross-sectional area A_r. Under this approximation, the resonators are tuned to a frequency $\omega_r(t) = c\sqrt{A_r(t)/Vl'}$ which also varies in time, with $l' = l + 1.7r$ being the effective neck length of a flanged resonator whose cylindrical neck has a radius r (Kinsler et al., 2000). The apparent input mass rate provided by a single resonator is given by $g = \rho A_r(t)\partial\psi/\partial t$, where ρ is the air density. Therefore, the expression for the total rate per unit volume accounting for a series of N resonators is expressed as:

$$G(x,t) = \sum_{j=1}^{N} \rho \frac{A_r}{A}\frac{\partial \psi_j}{\partial t}\delta\left(x - x_j\right), \tag{2}$$

where $\delta(x - x_j)$ is the delta function that accounts for the assumed point-wise action of the jth resonator placed at x_j. Substitution of 3 into 1 yields the equations of motion of the waveguide coupled with those of the resonators:

$$\begin{aligned} &\frac{1}{c^2}\frac{\partial^2 p}{\partial t^2} - \frac{\partial^2 p}{\partial x^2} = \rho\sum_{j=1}^{N}\left(\frac{A_r}{A}\frac{\partial^2 \psi_j}{\partial t^2} + \frac{1}{A}\frac{\partial A_r}{\partial t}\frac{\partial \psi_j}{\partial t}\right)\delta\left(x - x_j\right) \\ &m\frac{\partial^2 \psi_j}{\partial t^2} + \frac{\partial m}{\partial t}\frac{\partial \psi_j}{\partial t} + k\psi_j = -A_r p\left(x_j\right), \qquad j = 1, 2, \ldots, N \end{aligned} \tag{3}$$

where $m = \rho A_r l'$ and $k = \rho c^2 A_r^2/V$ are the effective mass and stiffness parameters of the resonators (Kinsler et al., 2000).

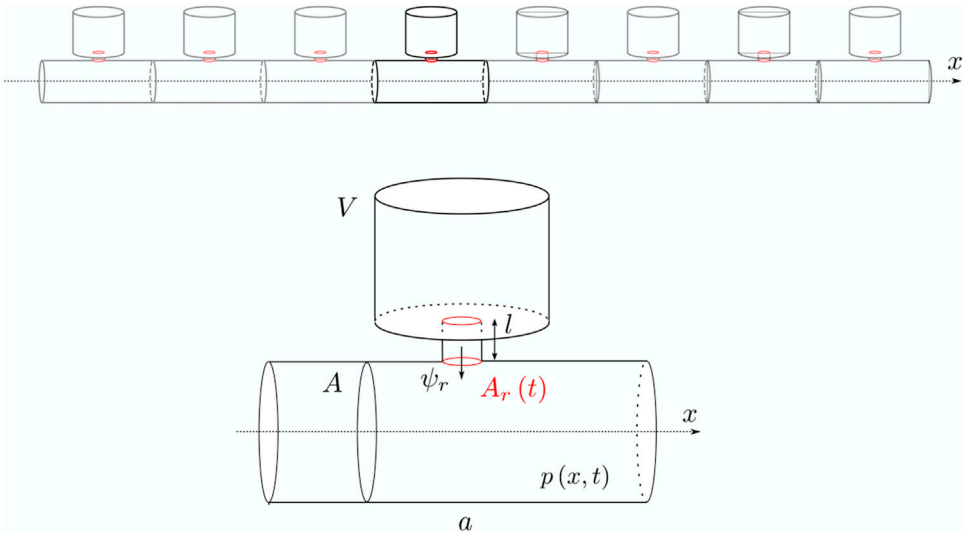

FIGURE 1
Schematic of the waveguide endowed with Helmholtz resonators, along with a zoomed view of the unit cell. The neck cross-section area A_r, highlighted in red, is modulated in time, while the other parameters are kept constant.

2.2 Dispersion calculation in the subwavelength regime

In order to investigate wave motion in the considered system and carry out analytical derivations, we now consider the homogenized version of Eq. 3, whereby the resonators are continuously distributed through the pipe:

$$\begin{aligned} \frac{1}{c^2}\frac{\partial^2 p}{\partial t^2}-\frac{\partial^2 p}{\partial x^2}&=\frac{\rho}{a}\left(\frac{A_r}{A}\frac{\partial^2\psi}{\partial t^2}+\frac{1}{A}\frac{\partial A_r}{\partial t}\frac{\partial\psi}{\partial t}\right)\\ m\frac{\partial^2\psi}{\partial t^2}+\frac{\partial m}{\partial t}\frac{\partial\psi}{\partial t}+k\psi&=-A_r p. \end{aligned} \tag{4}$$

Here, both $p(x,t)$ and $\psi(x,t)$ are now continuous functions of space and time. This approximation is accurate in the subwavelength regime, i.e., when the lattice size is much smaller than the wavelength ($a \ll \lambda$), and therefore there is a sufficiently dense distribution of resonators compared to the wavelength at the operating frequency. Eq. 4 is generally dependent upon the instantaneous value $A_r(t)$, and the rates $\partial A_r/\partial t$ and $\partial m/\partial t$. We first evaluate the dispersion in the time-invariant regime, i.e., assuming $\partial A_r/\partial t = 0$ and $\partial m/\partial t = 0$, with the area A_r considered as a free parameter. The obtained solutions form the basis for the adiabatic expansion under smooth temporal modulations derived in the next section. Therefore, we seek a plane wave solution of the form $p(x,t) = p_0 e^{i(\kappa x-\omega t)}$ and $\psi(x,t) = \psi_0 e^{i(\kappa x-\omega t)}$, where ω and κ are respectively angular frequency and wavenumber. Substitution into Eq. 4 yields the following dispersion relation:

$$\kappa = \pm\frac{\omega}{c}\sqrt{1+\frac{\mu}{1-\frac{\omega^2}{\omega_r^2}}} \tag{5}$$

where $\mu = V/aA$ is the volume ratio, i.e., the ratio between the volume enclosed in the resonator's chamber and the volume of the unit cell's pipe segment. Eq. 7 can be directly solved for $\omega(\kappa)$:

$$\omega = \pm\sqrt{\frac{c^2\kappa^2+\omega_r^2[1+\mu]}{2}\pm\sqrt{\left(\frac{c^2\kappa^2}{2}+\frac{\omega_r^2}{2}[1+\mu]\right)^2-c^2\kappa^2\omega_r^2}}. \tag{6}$$

Note that for any real-valued wavenumber κ, there are four solutions that define wave modes propagating in the pipe. The dispersion relation $\omega(\kappa)$ is illustrated in Figure 2A for two distinct conditions of A_r, corresponding to the initial and final modulation values $A_r^{(i)} = 10^{-5}\text{mm}^2$ (solid line) and $A_r^{(f)} = 5\cdot10^{-5}\text{mm}^2$ (dotted line) employed in the numerical part of the paper. Other relevant parameters of the resonator are $a = 16$ mm $l = 4$ mm, and $r = 8$ mm. In the figure, dimensionless frequencies $\Omega = \omega a/\pi c$ are used to highlight the subwavelength operational regime ($\Omega < 0.5$). Only two dispersion branches with positive frequencies Ω_1 and Ω_2 are shown in the figure, which define waves propagating to the right. The dispersion is symmetric about the wavenumber axis, with the two leftward propagating solutions $\Omega_{-2} = -\Omega_2$ and $\Omega_{-1} = -\Omega_1$ not shown in the figure for ease of visualization. The presence of the Helmholtz resonators breaks the typical linear dispersion curve of the pipe into two dispersion bands separated by a bandgap, whose bounds can be easily extracted from the analytical solutions. The lower bound $\omega_l = \omega_r$ takes the wavenumber κ to infinity in Eq. 7, while the upper bound $\omega_u = \omega_r\sqrt{1+\mu}$ is estimated by using $\kappa = 0$ in Eq. 6. We observe that the relative gap width $\Delta\omega/\omega_r = (\omega_u-\omega_l)/\omega_r = \sqrt{1+\mu}-1$ is determined solely by the resonator volume ratio μ, which plays a similar role to the mass ratio of mechanical resonators (Sugino et al., 2017). The examples in Figure 2A employ a fixed volume ratio of $\mu = 0.66$, and normalized tuning frequencies of $\Omega_r = 0.127$ and $\Omega_r = 0.23$ induced by the initial $A_r^{(i)}$ and final $A_r^{(f)}$ modulation values, respectively (note that the neck area does not influence the volume ratio μ). The analytical solution provided in Eq. 6 is valid in the subwavelength regime, and it's confirmed by comparison with numerical simulations in Section 3 that consider Eq. 3 without the subwavelength approximation. This solution is also compared to full 3D Finite Element (FE) simulations conducted

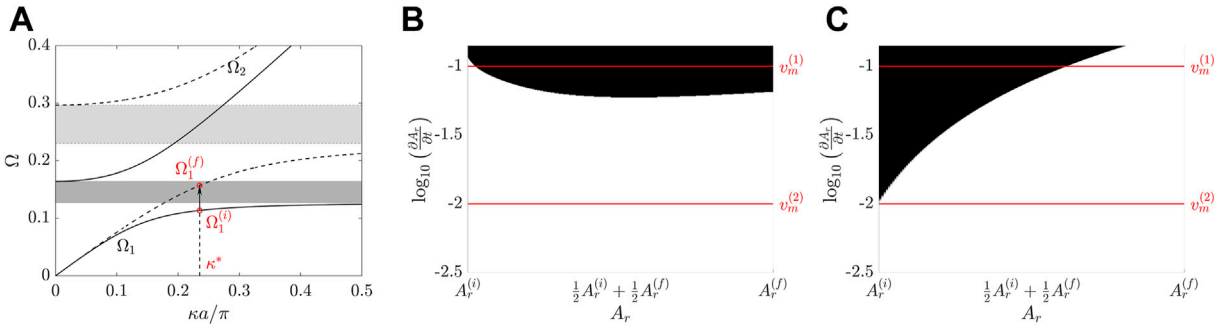

FIGURE 2
(A) Dispersion relation before (solid line) and after (dashed line) time-modulation. The gray boxes highlight the corresponding variation of the gap limits. The energy, provided with a central frequency Ω_1^i and wavenumber κ^*, undergoes an adiabatic transformation that follows the vertical arrow and is accompanied by frequency conversion from Ω_1^i to Ω_1^f. In contrast, non-adiabatic processes involve also other dispersion branches. **(B)** Limiting condition for adiabaticity in order for the wave mode $\Omega_1(\kappa^*)$ not to couple with the neighboring wave mode $\Omega_2(\kappa^*)$. The black region accommodates the values of A_r and $\partial A_r/\partial t$ for which the transformation can be considered non-adiabatic. **(C)** Limiting conditions for adiabaticity between wave modes Ω_1 and Ω_{-1}. The horizontal lines illustrate the constant velocity value used in the numerical simulations. $v_m^{(1)}$ corresponds to a non-adiabtic transformation, while $v_m^{(2)}$ corresponds to an adiabatic transformation.

within the COMSOL multiphysics environment in the Supplementary Material, which confirms the validity of the lumped parameter resonator approximation.

While here the area $A_r(t)$ is treated as a free parameter, its temporal variation modifies the dispersion properties of the pipe during wave propagation, producing a transformation that preserves the wavenumber content while promoting conversions of the frequency content across the modulation (Pacheco-Peña and Engheta, 2020a). We seek an adiabatic transformation represented with the black vertical arrow, whereby the energy initially injected in $\Omega_1^{(i)}(\kappa^*)$ follows the time evolution of the underlying dispersion until the value $A_r(t)$ reaches $A_r^{(f)}$, without triggering any energy conversion to other wave modes. In contrast, non-adiabatic transformations triggered by fast modulation protocols induce energy scattering to the neighboring wave modes that populate the dispersion at different frequencies $\Omega_j(\kappa^*)$. Note that, after time-modulation takes place, the energy is distributed among the frequencies of the final dispersion at the imposed wavanumber, i.e., $\Omega_j^{(f)}(\kappa^*)$, which are independent upon the modulation speed. Hence, the amount of frequency conversion can be designed solely based the resonators' initial and final configurations, and the associated dispersion properties. The modulation speed will in turn determine whether the modulation occurs with or without scattering to other wave modes, i.e., having a single or multiple output frequencies. In the following, we characterize these transformations in the light of the adiabatic theorem, which allows us to delineate the transition between waveguiding with and without scattering in time-varying acoustics.

2.3 Adiabatic transformations for slow temporal modulations

To investigate the time-varying dynamics caused by slow temporal variations of the area A_r, Eq. 4 is written in a first-order differential form by imposing only the wavenumber κ:

$$|\hat{z}_{,t}\rangle = H(\kappa, A_r(t))|\hat{z}\rangle \tag{7}$$

where $|\hat{z}\rangle = \left(\frac{\partial\hat{p}}{\partial t}, \frac{\partial\hat{\psi}}{\partial t}, \hat{p}, \hat{\psi}\right)^T$, (), t denotes a temporal derivative, and the time-dependent Hamiltonian matrix $H(\kappa, A_r(t))$ is:

$$H(\kappa, A_r(t)) = \begin{bmatrix} 0 & \mu\frac{\omega_r^2}{A_r}\frac{\partial m}{\partial t} - \frac{\rho c^2}{aA}\frac{\partial A_r}{\partial t} & -c^2\kappa^2 - \mu\omega_r^2 & \mu\frac{k\omega_r^2}{A_r} \\ 0 & -\frac{1}{m}\frac{\partial m}{\partial t} & \frac{A_r}{m} & -\omega_r^2 \\ 1 & 0 & 0 & 0 \\ 0 & 1 & 0 & 0 \end{bmatrix}. \tag{8}$$

This first-order differential form resembles Schrodinger's equations for quantum states where the adiabatic theorem is classically established [see for example, the book by Griffiths and Schroeter (2018), and also employed in multiple following studies due to its convenience in deriving adiabatic conditions (Amin, 2009; Tong, 2010). The ansatz $|\hat{z}\rangle = |\hat{z}_0\rangle e^{i\omega t}$ yields a time-dependent eigenvalue problem of the form $H(\kappa, A_r(t))|\hat{z}_j^R\rangle = i\omega_j|\hat{z}_j^R\rangle$, whose instantaneous solutions define the time-varying dispersion branches $\omega_j(\kappa, t)$ and associated eigenvectors $|\hat{z}\rangle^R(\kappa, t)$. In the case of smooth modulations produced by small rates of change of the area $A_r(t)$, these instantaneous solutions correspond to those obtained in Eq. 6 where A_r is treated as a free parameter. Hence, the solutions define the four time-dependent waves that can propagate in the pipe, and form a natural basis for the expansion of the total solution:

$$|\hat{z}\rangle(t) = \sum_j c_j(t)|\hat{z}_j^R\rangle(t)e^{i\theta_j}, \qquad j = [-2, -1, 1, 2], \tag{9}$$

where $\theta_j = \int_0^t \omega_j(\tau)d\tau$ is the geometric phase, which replaces the ωt term commonly present in time-independent solutions, and $c_j(t)$ are the time-dependent participation factors for each wave mode. Plugging the solution into Eq. 7 and performing a series of algebraic manipulations (Santini and Riva, 2022) yields the following differential equation that describes the time evolution of the participation factor $c_r(t)$:

$$c_{r,t} = -\langle\hat{z}_r^L|\hat{z}_{r,t}^R\rangle\, c_r - \sum_{j\neq r}\frac{\langle\hat{z}_r^L|H_{,t}|\hat{z}_j^R\rangle}{i\left(\omega_j - \omega_r\right)}c_j e^{i\left(\theta_j - \theta_r\right)}, \tag{10}$$

where $\langle z_r^L|(t)$ is the left eigenvector. For a given initial condition defined by a combination of propagating modes, these equations can be solved to obtain the time evolution of each participation factor $c_r(t)$. While that is not always convenient, the equations are particularly useful to derive the conditions for adiabatic transformations in which the evolution occurs through an isolated mode. Suppose for example, that energy is initially inserted in a single mode r, i.e., $c_r(0) = 1$ and $c_j(0) = 0$ for $j \neq r$. In order for the participation factor $c_r(t)$ to remain the only non-zero term, its coupling to the other modes, represented by the right-most term in Eq. 10 must remain small and, therefore, the following integral must be negligible:

$$\int_0^t \sum_{j\neq r} \frac{\langle \hat{z}_r^L|H_{,\xi}|\hat{z}_j^R\rangle}{\mathrm{i}\left(\omega_j-\omega_r\right)} c_j \mathrm{e}^{\mathrm{i}\left(\theta_j-\theta_r\right)} d\xi = -\sum_{j\neq r} \frac{\langle \hat{z}_r^L|H_{,\xi}|\hat{z}_j^R\rangle}{\left(\omega_j-\omega_r\right)^2} c_j \mathrm{e}^{\mathrm{i}\left(\theta_j-\theta_r\right)}\Bigg|_0^t + \int_0^t \frac{d}{d\xi}\left(\sum_{j\neq r} \frac{\langle \hat{z}_r^L|H_{,\xi}|\hat{z}_h^R\rangle}{\left(\omega_j-\omega_r\right)^2} c_j \mathrm{e}^{\mathrm{i}\left(\theta_j-\theta_r\right)}\right) d\xi. \tag{11}$$

Since the second term on the right-hand side (obtained through integration by parts) is negligible (Ibáñez and Muga, 2014), we arrive at the following condition:

$$\left|\frac{\langle \hat{z}_j^L|H_{,t}|\hat{z}_r^R\rangle}{\left(\omega_h-\omega_r\right)^2}\right| \ll 1. \tag{12}$$

The condition in Eq. 12 is employed to analyze the coupling between the imposed wave mode and the other modes which may be involved in the solution. The condition must be evaluated for a given pair of wave modes and a certain imposed wavenumber. To exemplify, we consider the imposed wavenumber k^* and solution Ω_1 marked in Figure 2A, and we quantify the coupling to the solution Ω_2 and to the left-propagating solution $\Omega_{-1} = -\Omega_1$ in Figures 2B, C, respectively. We evaluate the norm in Eq. 12 as a function of A_r and its rate of change (i.e., modulation speed) $v_m = \partial A_r/\partial t$, marking with black the regions that surpass a chosen threshold value of 0.01. The plots, therefore, serve as maps which mark adiabatic (white) and non-adiabatic (black) regions as a function of A_r and v_m. Two horizontal lines for representative velocity values $v_m^{(1)} = 0.1$ mm^2/s and $v_m^{(2)} = 0.01$ mm^2/s are displayed in the figure, illustrating two extreme cases that promote non-adiabatic and adiabatic transformations. The behavior for these modulation speeds is further demonstrated by the numerical simulations in the next section, illustrating the presence and absence of scattering to other wave modes.

3 Numerical results

In this section, we present a few case studies to elucidate the role of time modulation in the considered acoustic metamaterials, with emphasis on frequency conversion, mode conversion, and the derived adiabatic conditions. The results are obtained through numerical simulations performed through a finite difference time domain (FDTD) algorithm, where the partial derivatives in Eq. 3 are discretized through a central difference approximation, and absorbing conditions are added to the boundaries to mitigate reflections. For simplicity, we employ a piecewise linear variation of the neck cross-section area:

$$A_r(t) = \begin{cases} A_r^{(i)} & t < t_i \\ A_r^{(i)} + v_m(t-t_i) & t_i < t < t_f \\ A_r^{(f)} & t > t_f \end{cases} \tag{13}$$

Where t_i and t_f are the start and finish time instants for the modulation, and v_m is the constant modulation velocity. In the simulations, a sinusoidal wave packet with $n = 30$ periods is imposed through a prescribed velocity to the left end of a finite waveguide of length L. We remark that the wavepacket propagates at a speed given by the group velocity $c_g = \partial\omega/\partial\kappa$, which is evaluated at the impinging wavenumber κ and angular frequency $\omega(\kappa, t)$, and therefore varies in time. The distance traveled by the wavepacket at an arbitrary time T is calculated by the integral $\int_0^T c_{g_1}(\kappa^*)dt$, where c_g is the group velocity relative to the impinging state $\Omega_1(t)$, evaluated for the incident wavenumber $\kappa^* = 2\pi/\lambda^*$ with corresponding wavelength λ^*. In the following simulations, we employ a waveguide of length $L/\lambda^* \approx 34$, which we estimate to be sufficiently long in order to observe the time history of interest. The excitation occurs within the time-invariant window $t < t_i$, establishing a propagating wave packet with a desired frequency/wavenumber spectral content according to the dispersion at the initial state $A_r = A_r^{(i)}$. We hereafter present the following representative examples: (i) a fast (non-adiabatic) modulation with $v_m = v_m^{(1)}$, which allows increasing the frequency content of an impinging wave packet while compressing its time envelope. Such a non-adiabatic process is accompanied by energy leakage toward the other states supported by the waveguide, (ii) a slow (adiabatic) modulation with $v_m = v_m^{(2)}$ able to perform frequency up-conversion and compression of an impinging wave packet, but without any energy leakage toward other wave modes.

The time history relative to example (i) is displayed in Figure 3A. The excitation is provided with a central frequency $\Omega_1^{(i)} = \Omega_1(\kappa^*) = 0.109$, targeting the lower dispersion branch of Figure 2A in the nearly-flat region close to the resonance, which exhibits limited group velocity and highly dispersive characteristics. This region is chosen as it exhibits a large change with respect to the final dispersion branch (dashed lines in Figure 2A) for the imposed wavenumber. In this example, the modulation takes place in a non-adiabatic manner due to the high modulation speed $v_m^{(1)}$, and the energy content is leaked to other available states supported by the waveguide. Indeed, wave motion in Figure 3A exhibits sharp changes after time modulation, with distinct wave packets of different amplitude and speeds emerging. To better elucidate this concept, we report the wave packets before (black curves) and after (red curves) time modulation. Figure 3B illustrates the spatial envelope of the wave and its wavenumber content, evaluated at fixed time instants (marked with dots in Figure 3A). We note that, as expected of temporal modulations and discontinuities (Pacheco-Peña and Engheta, 2020b), the wavelength and associated wavenumber content are preserved throughout the process. In contrast, the corresponding frequency content undergoes transformations, as illustrated in Figure 3C which displays the time and frequency representation of the wave packet for fixed spatial positions before and after time modulation. We note that the main frequency component of the wave packet undergoes a frequency shift toward a higher frequency $\Omega_1^{(f)}$, and its spectral width broadens after time modulation, which corresponds to a compression of the time-domain signal. An additional frequency

10.3389/facou.2023.1271221

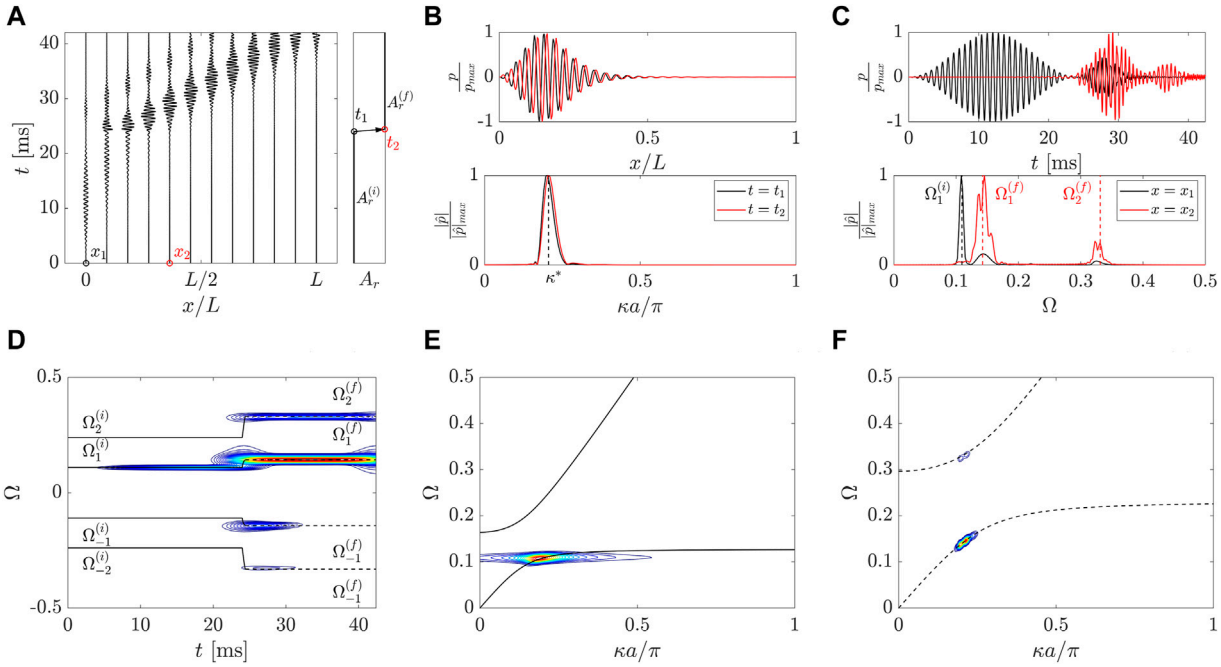

FIGURE 3
(A) Wavefield $p(x, t)$ obtained through a non-adiabatic modulation velocity $v_m^{(1)}$, which is graphically represented in the waterfall plot. In the figure, x_1, x_2, t_1, and t_2 are used to mark the space and time coordinates used to produce the plots in Figs. **(B,C)**. **(B)** Pressure field and corresponding wavenumber content evaluated at constant time instants t_1 and t_2 before (black curve) and after (red curve) time modulation. The wavenumber is preserved across the time discontinuity. **(C)** Pressure field and corresponding frequency spectrum evaluated at prescribed coordinates x_1 and x_2. A frequency conversion mechanism takes place, whereby the impinging energy is split over multiple and distinct frequencies. **(D)** Frequency spectrogram evaluated over time. The colored contours represent the energy that is injected to excite Ω_1 and is frequency-converted into different wavemodes Ω_j. The black curves represent the expected evolution of the states in time. **(E,F)** Comparison between dispersion relation and 2D FFTs of the wavefield **(E)** before and **(F)** after time modulation.

component centered at $\Omega_2^{(f)}$ is also noted after the time modulation due to the scattering caused by the non-adiabatic process.

To better illustrate the frequency transformations, we present a frequency spectrogram in Figure 3D, which is evaluated by windowing the pressure field $p(x,t)$ with a moving Gaussian function $G(t) = e^{-(t-t_0)^2/2c_0^2}$. Here,$c_0 = 0.06T_f$ determines the width of the Gaussian and t_0 is its central value, which is smoothly varied to produce the spectrogram within the interval $t_0 \in [0, t_f]$. For ease of visualization, the Fourier-transformed pressure field $\hat{p}(\kappa, f, t_0)$ is further processed by taking the RMS value along κ, which eliminates one dimension. The resulting spectrogram $|\hat{p}(f, t_0)|$ in Figure 3D is overlaid to black curves that represent the wave modes $\Omega_j(\kappa^*)$ supported by the waveguide at the incident wavenumber κ^*. As expected, the energy content is initially concentrated in the branch $\Omega_1^{(i)}$ and is mainly converted through the evolution of that branch to $\Omega_1^{(f)}$. Due to the non-adiabatic transformation, other wave modes are present after modulation: the second branch $\Omega_2^{(f)}$ significantly contributes to the wave motion, and minor contributions are also observed for $\Omega_{-1}^{(f)}$ and $\Omega_{-2}^{(f)}$, generating back-propagating waves. Note that around t = 30 ms the back-propagating waves are reflected off the left boundary and converted back into the right propagating modes Ω_1 and Ω_2. Finally, Figures 3E, F display the 2D Fourier Transforms of the pressure field before and after time modulation, overlaid to the numerical dispersion curves for the initial and final states. These diagrams confirm that frequency conversion follows the underlying dispersion, with energy initially concentrated in the excited first branch, and afterward leaked also to the second branch. Due to the wavenumber-preserving transformation, the output frequency content of the first branch has a wider spectrum when compared to the input, which explains the time compression of that portion of the signal evidenced in Figure 3C. In this case, the frequency shift and signal compression are observable but contaminated with energy from other wave modes due to the non-adiabatic-induced scattering.

A cleaner frequency conversion and signal compression are demonstrated in the second example (ii) corresponding to a modulation velocity $v_m^{(2)} < v_m^{(1)}$, which triggers an adiabatic evolution of the state dictated by the underlying conversion mechanism and described by the black vertical arrow in Figure 2A. As such, the time history in Figure 4A evidences a single wave packet that transforms with minimal scattering toward other states. This is confirmed by the space snapshot and time evolution of the wave packets reported in Figures 4B, C, along with corresponding wavenumber and frequency representations. In absence of further wave modes, Figure 4B illustrates the same wavenumber conservation as in example (i), while 4(c) displays a frequency conversion and compression mechanisms of the impinging wave packet. In addition, the spectrogram in Figure 4D confirms the evolution through the single branch corresponding to Ω_1, while the dispersion plots in Figures 4E, F confirm that the spectral content obeys the predicted behavior of the initial and final states, with no scattering to other wave modes. Finally, we note that in experimental implementations it may be important to estimate the minimum waveguide length necessary to observe an

10.3389/facou.2023.1271221

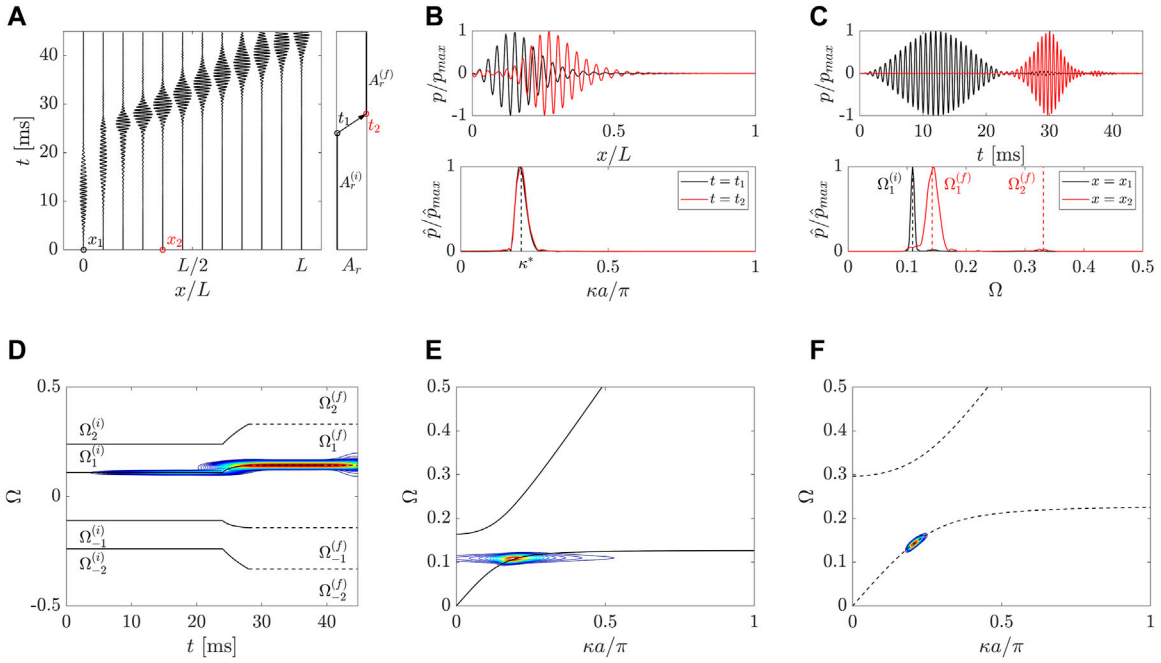

FIGURE 4
(A) Wavefield $p(x, t)$ for an adiabatic transformation driven by a sufficiently slow modulation velocity $v_m^{(2)}$. **(B)** Pressure distribution in space $p(x)$ and corresponding wavenumber content $\hat{p}(\kappa)$ measured before (black curve) and after (red curve) time modulation. **(C)** Pressure distribution in time $p(t)$ and frequency content $\hat{p}(\Omega)$ probed at constant positions x_1 and x_2. The time domain signal exhibits compression of the wavepacket, which is consistent with a broader spectral content. **(D)** Corresponding frequency spectrogram with superimposed evolution of the underlying wave modes Ω_j. Due to the adiabatic transformation, the energy content does not leak toward the neighboring states and remains located in correspondence of Ω_1. **(E,F)** Comparison between dispersion relation and 2D FFTs of the wavefield **(E)** before and **(F)** after time modulation.

adiabatic transition. This is because the modulation has a limiting speed, and therefore the wavepacket must be traveling within the waveguide without experiencing reflections for the duration of the modulation. As previously described, the distance traveled by the wavepacket can be estimated by integrating the group velocity, which must include the initial duration $t = 0 \rightarrow t_i$ required to create the wavepacket, and the duration of the time modulation $t = t_i \rightarrow t_f$, here resulting in a distance of $L_{min} = \int_0^{t_f} c_{g_1}(\kappa^\star)dt = 13.7\lambda^\star$. Naturally, we guaranteed that the total waveguide length in our simulations was larger than this minimum to observe the adiabatic transitions.

4 Conclusion

In this paper, we have explored the dynamics of acoustic metamaterials endowed with time-varying Helmholtz resonators. When a sound wave propagates simultaneously to a temporal modulation, the wave packet experiences a frequency conversion dictated by the underlying dispersion, which may result in signal compression or dilation. If the speed of the modulation is fast, or non-adiabatic, the time evolution of the wave packet can be accompanied by energy scattering to other wave modes. In contrast, sufficiently slow modulations can frequency transform the impinging wave in an adiabatic manner and without any energy leak to the other dispersion branches. We have established the limiting condition for the modulation speed to distinguish between adiabatic and non-adiabatic processes. The developed framework, illustrated through selected numerical case studies, is generally applicable to a variety of time-varying metamaterial systems. Therefore, the presented results may open new opportunities in time-varying acoustics with application to signal processing, sound isolation, and energy conversion. Future investigations will focus on the experimental validation of the concepts herein explored, where time-varying resonators can be achieved through mechanical opening and closure of the apertures. Similar approaches have been used in the context of acoustic topological pumping for example, by the relative translation of two incommensurate waveguides (Cheng et al., 2020) or dynamic boundary changes through rotation mechanisms (Xu et al., 2020).

Data availability statement

The raw data supporting the conclusion of this article will be made available by the authors, without undue reservation.

Author contributions

ER: Formal Analysis, Investigation, Software, Visualization, Writing–original draft. MRo: Conceptualization, Investigation, Software, Visualization, Writing–original draft. YG: Conceptualization, Investigation, Software, Visualization, Writing–original draft, Writing–review and editing. MRu: Conceptualization, Funding acquisition, Writing–review and editing.

Funding

The author(s) declare that no financial support was received for the research, authorship, and/or publication of this article.

Conflict of interest

The authors declare that the research was conducted in the absence of any commercial or financial relationships that could be construed as a potential conflict of interest.

The authors MRu and ER declared that they were editorial board members of Frontiers at the time of submission. This had no impact on the peer review process and the final decision.

Publisher's note

Supplementary material

The Supplementary Material for this article can be found online at: https://www.frontiersin.org/articles/10.3389/facou.2023.1271221/full#supplementary-material

References

Allam, A., Sabra, K., and Erturk, A. (2021). Sound energy harvesting by leveraging a 3d-printed phononic crystal lens. *Appl. Phys. Lett.* 118, 103504. doi:10.1063/5.0030698

Amin, M. H. (2009). Consistency of the adiabatic theorem. *Phys. Rev. Lett.* 102, 220401. doi:10.1103/physrevlett.102.220401

Chen, Y., Liu, H., Reilly, M., Bae, H., and Yu, M. (2014). Enhanced acoustic sensing through wave compression and pressure amplification in anisotropic metamaterials. *Nat. Commun.* 5, 5247. doi:10.1038/ncomms6247

Cheng, W., Prodan, E., and Prodan, C. (2020). Experimental demonstration of dynamic topological pumping across incommensurate bilayered acoustic metamaterials. *Phys. Rev. Lett.* 125, 224301. doi:10.1103/physrevlett.125.224301

Cummer, S. A., Christensen, J., and Alù, A. (2016). Controlling sound with acoustic metamaterials. *Nat. Rev. Mater.* 1, 16001–16013. doi:10.1038/natrevmats.2016.1

De Ponti, J. M., Colombi, A., Riva, E., Ardito, R., Braghin, F., Corigliano, A., et al. (2020). Experimental investigation of amplification, via a mechanical delay-line, in a rainbow-based metamaterial for energy harvesting. *Appl. Phys. Lett.* 117, 143902. doi:10.1063/5.0023544

De Ponti, J. M., Iorio, L., Riva, E., Ardito, R., Braghin, F., and Corigliano, A. (2021). Selective mode conversion and rainbow trapping via graded elastic waveguides. *Phys. Rev. Appl.* 16, 034028. doi:10.1103/physrevapplied.16.034028

Dong, H.-W., Zhao, S.-D., Oudich, M., Shen, C., Zhang, C., Cheng, L., et al. (2022). Reflective metasurfaces with multiple elastic mode conversions for broadband underwater sound absorption. *Phys. Rev. Appl.* 17, 044013. doi:10.1103/physrevapplied.17.044013

Griffiths, D. J., and Schroeter, D. F. (2018). *Introduction to quantum mechanics*. Cambridge: Cambridge University Press.

Grinberg, I. H., Lin, M., Harris, C., Benalcazar, W. A., Peterson, C. W., Hughes, T. L., et al. (2020). Robust temporal pumping in a magneto-mechanical topological insulator. *Nat. Commun.* 11, 974. doi:10.1038/s41467-020-14804-0

Hu, G., Tang, L., Liang, J., Lan, C., and Das, R. (2021). Acoustic-elastic metamaterials and phononic crystals for energy harvesting: A review. *Smart Mater. Struct.* 30, 085025. doi:10.1088/1361-665x/ac0cbc

Hussein, M. I., Leamy, M. J., and Ruzzene, M. (2014). Dynamics of phononic materials and structures: Historical origins, recent progress, and future outlook. *Appl. Mech. Rev.* 66. doi:10.1115/1.4026911

Ibáñez, S., and Muga, J. (2014). Adiabaticity condition for non-hermitian hamiltonians. *Phys. Rev. A* 89, 033403. doi:10.1103/physreva.89.033403

Kadic, M., Milton, G. W., van Hecke, M., and Wegener, M. (2019). 3d metamaterials. *Nat. Rev. Phys.* 1, 198–210. doi:10.1038/s42254-018-0018-y

Kinsler, L. E., Frey, A. R., Coppens, A. B., and Sanders, J. V. (2000). *Fundamentals of acoustics*. China: John Wiley & Sons.

Liu, Z., Zhang, X., Mao, Y., Zhu, Y., Yang, Z., Chan, C. T., et al. (2000). Locally resonant sonic materials. *science* 289, 1734–1736. doi:10.1126/science.289.5485.1734

Ma, G., Xiao, M., and Chan, C. T. (2019). Topological phases in acoustic and mechanical systems. *Nat. Rev. Phys.* 1, 281–294. doi:10.1038/s42254-019-0030-x

Marconi, J., Riva, E., Di Ronco, M., Cazzulani, G., Braghin, F., and Ruzzene, M. (2020). Experimental observation of nonreciprocal band gaps in a space-time-modulated beam using a shunted piezoelectric array. *Phys. Rev. Appl.* 13, 031001. doi:10.1103/physrevapplied.13.031001

Miniaci, M., Pal, R., Morvan, B., and Ruzzene, M. (2018). Experimental observation of topologically protected helical edge modes in patterned elastic plates. *Phys. Rev. X* 8, 031074. doi:10.1103/physrevx.8.031074

Norris, A. N. (2008). Acoustic cloaking theory. *Proc. R. Soc. A Math. Phys. Eng. Sci.* 464, 2411–2434. doi:10.1098/rspa.2008.0076

Oudich, M., Gerard, N. J., Deng, Y., and Jing, Y. (2023). Tailoring structure-borne sound through bandgap engineering in phononic crystals and metamaterials: A comprehensive review. *Adv. Funct. Mater.* 33, 2206309. doi:10.1002/adfm.202206309

Pacheco-Peña, V., and Engheta, N. (2020a). Antireflection temporal coatings. *Optica* 7, 323–331. doi:10.1364/optica.381175

Pacheco-Peña, V., and Engheta, N. (2020b). Temporal aiming. *Light Sci. Appl.* 9, 129. doi:10.1038/s41377-020-00360-1

Pal, R. K., and Ruzzene, M. (2017). Edge waves in plates with resonators: an elastic analogue of the quantum valley hall effect. *New J. Phys.* 19, 025001. doi:10.1088/1367-2630/aa56a2

Santini, J., and Riva, E. (2022). Elastic temporal waveguiding. *New J. Phys.* 25, 013031. doi:10.1088/1367-2630/acb45d

Sugino, C., Xia, Y., Leadenham, S., Ruzzene, M., and Erturk, A. (2017). A general theory for bandgap estimation in locally resonant metastructures. *J. Sound Vib.* 406, 104–123. doi:10.1016/j.jsv.2017.06.004

Süsstrunk, R., and Huber, S. D. (2015). Observation of phononic helical edge states in a mechanical topological insulator. *Science* 349, 47–50. doi:10.1126/science.aab0239

Tong, D. (2010). Quantitative condition is necessary in guaranteeing the validity of the adiabatic approximation. *Phys. Rev. Lett.* 104, 120401. doi:10.1103/physrevlett.104.120401

Trainiti, G., and Ruzzene, M. (2016). Non-reciprocal elastic wave propagation in spatiotemporal periodic structures. *New J. Phys.* 18, 083047. doi:10.1088/1367-2630/18/8/083047

Trainiti, G., Xia, Y., Marconi, J., Cazzulani, G., Erturk, A., and Ruzzene, M. (2019). Time-periodic stiffness modulation in elastic metamaterials for selective wave filtering: Theory and experiment. *Phys. Rev. Lett.* 122, 124301. doi:10.1103/physrevlett.122.124301

Tsakmakidis, K. L., Boardman, A. D., and Hess, O. (2007). 'trapped rainbow'storage of light in metamaterials. *Nature* 450, 397–401. doi:10.1038/nature06285

Wang, X., Li, J., Yang, J., Chen, B., Liu, S., and Chen, Y. (2023). Compact acoustic amplifiers based on non-adiabatic compression of sound in metamaterial waveguides. *Appl. Acoust.* 204, 109246. doi:10.1016/j.apacoust.2023.109246

Xia, Y., Riva, E., Rosa, M. I., Cazzulani, G., Erturk, A., Braghin, F., et al. (2021). Experimental observation of temporal pumping in electromechanical waveguides. *Phys. Rev. Lett.* 126, 095501. doi:10.1103/physrevlett.126.095501

Xu, X., Wu, Q., Chen, H., Nassar, H., Chen, Y., Norris, A., et al. (2020). Physical observation of a robust acoustic pumping in waveguides with dynamic boundary. *Phys. Rev. Lett.* 125, 253901. doi:10.1103/physrevlett.125.253901

Zangeneh-Nejad, F., and Fleury, R. (2019). Active times for acoustic metamaterials. *Rev. Phys.* 4, 100031. doi:10.1016/j.revip.2019.100031